Available online at www.sciencedirect.com
ScienceDirect
Journal of Nuclear Materials 357 (2006) 147–155
journal of nuclear materials
www.elsevier.com/locate/jnucmat

EBSP measurements of hydrogenated Zircaloy-2 claddings with stress-relieved and recrystallized annealing conditions

Katsumi Une *, Shinji Ishimoto

Nippon Nuclear Fuel Development Co., Ltd., 2163, Oarai-machi, Narita-cho, Higashi-ibaraki-gun, Ibaraki-ken 311-1313, Japan

Received 7 April 2006; accepted 6 June 2006

Abstract

Precipitation behavior of zirconium hydrides and microscopic texture in three kinds of Zircaloy-2 fuel claddings with stress-relieved and recrystallized annealing conditions have been examined by electron backscattering diffraction patterns (EBSP). The microscopic texture data obtained by EBSP were consistent with the macroscopic X-ray data. The zirconium basal plane was observed to have a more radial texture in the case of the recrystallized tube as compared to the stress-relieved tube, even though both tubes had the same tube reduction path. In the recrystallized tubes, the frequency of precipitation and stable growth sites in inter-granular hydrides were about twice as high as that in intra-granular sites. In the stress-relieved tubes, this value was not calculated because of the almost equivalent sizes of hydrides and smaller zirconium matrix grains. The observation frequency of the habit planes of hydrides, which was statistically derived based on pole figure analysis of EBSP between hydrides and surrounding zirconium matrix grains, decreased in the order $(0001)_\alpha \| \{111\}_\delta \gg \{10\bar{1}7\}_\alpha \| \{111\}_\delta > \{10\bar{1}1\}_\alpha \| \{110\}_\delta$.

PACS: 28.41.Bm; 68.55.Ac; 68.55.Jk

1. Introduction

Zirconium alloy fuel cladding used in light water reactors picks up hydrogen during operation through a corrosion reaction with coolant water. When the hydrogen concentration in the cladding exceeds the terminal solid solubility, zirconium hydride is precipitated, which reduces the ductility of the cladding. In particular, radially oriented hydrides drastically reduce the circumferential ductility. Indeed, occurrences of unfavorable cracking have been observed in Zr alloys in reactor operations of normal, transient and accident cases: delayed hydride cracking (DHC) in Zr–2.5%Nb pressure tubes of CANDU reactor [1,2], secondary degraded cracking in BWR claddings after primary fuel failure [3,4], outside-in type cracking in high burnup BWR claddings arising at power ramp tests [5,6], and hydride-assisted pellet cladding mechanical interaction (PCMI) type cracking of PWR and BWR claddings under reactivity-initiated accident (RIA) situations [7,8].

Zirconium alloy cladding tubes are fabricated from tube-shells through several cold-reduction

* Corresponding author. Tel.: +81 29 267 9011; fax: +81 29 267 9014.
E-mail address: une@nfd.co.jp (K. Une).

0022-3115/$ - see front matter © 2006 Elsevier B.V. All rights reserved.
doi:10.1016/j.jnucmat.2006.06.004

and annealing schedules, and subjected to a final annealing process. Consequently, various properties of the cladding tubes, such as mechanical and physical properties, and the irradiation behavior of corrosion, hydrogen pickup, irradiation growth, and so on, are mainly dependent on the tube reduction process and final annealing temperature. The precipitation behavior of the hydrides depends strongly on these two fabrication parameters because δ-ZrH_x precipitates preferentially on a certain habit plane of the unit cell of the hcp α-Zr, and the cladding tubes have a strong crystallographic texture. More radially textured tubes of the basal plane have more circumferentially oriented hydrides [9–11]. Different precipitation morphology of hydrides is frequently observed between stress-relieved and recrystallized tubes, presumably due to the different grain structures and texture [12].

There has been ongoing research to determine the crystallography of Zr hydrides by metallographic trace, X-ray diffraction (XRD) and transmission electron microscopy (TEM). Through these techniques, various hydride habit planes have been reported: the prism plane of $\{10\bar{1}0\}$ [9,13–15], the twinning planes of $\{10\bar{1}2\}$, $\{11\bar{2}1\}$ and $\{11\bar{2}2\}$ [16], the pyramidal plane of $\{10\bar{1}1\}$ [17–19], the basal plane of (0001) [12,17,19–23], and the $\{10\bar{1}7\}$ plane [9,15,24,25]. This ambiguity in the results may be attributed to not only experimental difficulty in determining the crystallographic relationship between the hydrides and matrix grains, but also the variety of fabrication processes and heat treatments of the materials used. Thus, the evaluation of hydride precipitation behavior based on statistical amounts of crystallographic data are needed for Zircaloy cladding tubes with different textures and grain structures.

In our previous study [26], we have succeeded in the application of electron backscattering diffraction patterns (EBSP) for the acquisition of crystallographic data on the hydrides and Zr matrix for a current recrystallized Zircaloy-2 cladding tube with an average grain size of about 3 μm. The EBSP could effectively determine the precipitation morphology and crystallographic orientations of the hydrides, both in the grains and along the grain boundaries. Moreover, we proposed a qualitative reorientation mechanism of hydrides induced by tensile stress, based on the data of radially oriented hydrides. In this subsequent study, EBSP measurements were applied to the analysis of hydride precipitation behavior in stress-relieved cladding tubes with smaller grains and higher lattice strains, as well as two other recrystallized cladding tubes supplied by different tube vendors. From the EBSP mapping data and statistical amounts of crystallographic data, the precipitation behavior and hydride habit planes in these tubes were compared in terms of grain structure and texture effects.

2. Experimental

2.1. Specimen

The three kinds of Zircaloy-2 cladding tubes examined in the present EBSP measurements have the same tube size: outside diameter, 11.2 mm; wall thickness, 0.71 mm, lined with pure Zr (liner thickness: 0.08 mm). The alloy compositions of Zircaloy-2 were 1.37 Sn, 0.17 Fe, 0.11 Cr and 0.07 Ni in wt%. The final heat treatment after cold rolling was performed in two steps of 577 °C × 2 h yielding a recrystallized grain structure, and 480 °C × 3 h yielding a stress-relieved grain structure. Table 1 tabulates specimen identification and final annealing conditions for the three tubes. The two recrystallized tubes, RX1 and RX2, were supplied by different tube vendors. The stress-relieved tube, SR1, was prepared by annealing a cold-worked tube fabricated through the same process as RX1 except for

Table 1
Annealing condition, grain size and microtexture of Zircaloy-2 cladding tubes evaluated by EBSP

Specimen	Heat treatment	Zircaloy grain size (μm)	Fraction of low angle boundary (%)[a]	Radial texture parameter (%)[b]	f_r value by XRD
RX1	577 °C × 2 h	2.8	5.9	60	0.62
RX2	577 °C × 2 h	2.9	5.2	67	0.64
RX3[c]	577 °C × 2 h	–	–	–	0.62[c]
SR1	480 °C × 2 h	1.0	25.5	44	–

[a] Grain misorientation angle: 5–15°.
[b] Fraction of Zr grains whose basal poles are tilted within ±40° from the tube radial direction.
[c] Ref. [26]; f_r value by EBSP: 0.60.

the final annealing and tube straightening processes. The recrystallized RX3 tube in Table 1, which was supplied from the third vendor, had been examined in our first EBSP measurements [26].

The present three tube specimens (RX1, RX2, SR1) were hydrogenated in LiOH solution at 290 °C for 135 h followed by cooling at a rate of about 0.5 °C/min. Fig. 1 shows optical micrographs of the specimens after the etching treatment. Many strings of circumferentially oriented hydrides are precipitated on the outside and middle sections of the Zircaloy-2 claddings. A region depleted of hydrides is seen in the portion of Zircaloy-2 adjacent to the Zr liner region, and a highly heterogeneous precipitation of hydrides is seen in the Zr liner region. These are basically caused by the difference in the terminal solid solubility of hydrogen between Zircaloy-2 and pure Zr [27,28]. The average hydrogen concentration of the specimen analyzed by the hot vacuum extraction method was around 200–300 ppm, including the hydrogen in the Zr liner region.

2.2. EBSP measurements

The final surface treatment of polished samples for EBSP mapping was carried out by electropolishing in a solution of 20% $HClO_4$ and 80% C_2H_5OH, followed by an ion-milling procedure. The procedure for EBSP specimen preparation was described in detail previously [26]. Crystallographic orientation measurements in cross-sectioned cladding of the circumferential–radial plane were made using a FE-SEM (JSM6500F) equipped with an EBSP system (TSL-OIM). The estimated diameter of the electron beam at an acceleration voltage of 20 kV and a probe current of 1.5 nA was about 0.02 μm and the scanning step adopted for EBSP mapping was always 0.1 μm. The relationship of crystallographic orientation between the hydrides and the surrounding Zr matrix grains was evaluated by normal pole figure plots of the Zr matrix and hydride phases at each analysis point.

3. Results and discussion

3.1. Grain structure and microtexture

In this section, EBSP results regarding the grain structure and microtexture of the Zircaloy matrix are described. Since the temperature during the hydrogenation treatment of the three kinds of tubes was rather low of 290 °C, it is reasonably assumed that the precipitation of Zr hydrides in the matrix did not affect the grain structure and microtexture.

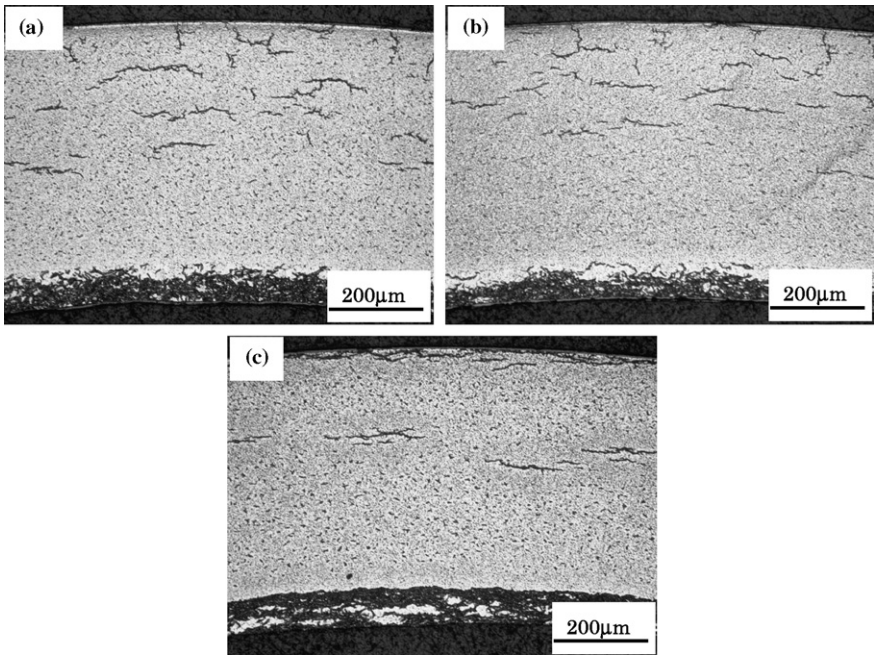

Fig. 1. Optical micrographs of hydrogenated Zircaloy-2 cladding tubes: (a) RX1, (b) RX2, (c) SR1.

The Kikuchi patterns indexed by the EBSP system for the matrix and hydrides show α-Zr of the hcp structure and δ-ZrH_x of the fcc structure. Figs. 2(a)–(c) and 3(a)–(c) show examples of image quality (IQ) maps and crystal orientation maps of α-Zr for the two types of recrystallized tubes (RX1, RX2) and the stress-relieved tube (SR1), which were obtained with an EBSP scanning step of 0.1 μm. The IQ maps of the two recrystallized tubes show relatively high lattice strains in the grain boundaries and the interfaces between hydrides and Zr matrix. The IQ map of the stress-relieved tube shows very high lattice strains or high density of dislocations, in which a large number of bright and small grains in a partly recrystallized state were observed.

In the crystal orientation maps of Fig. 3(a)–(c), each α-Zr grain is categorized into three different gray levels, which represent the tilt angle ranges of the basal pole from the radial direction of the tube: (1) 0–30°, (2) 30–60 ° and (3) 60–90 °. Lighter grains have more radial orientations of the basal pole. Yellow grains in the maps, which are interconnected and roughly oriented toward the circumferential direction of the tube in a zigzag manner, are δ-ZrH_x phase. The black and red lines in the maps represent high- and low angle grain boundaries with misorien-

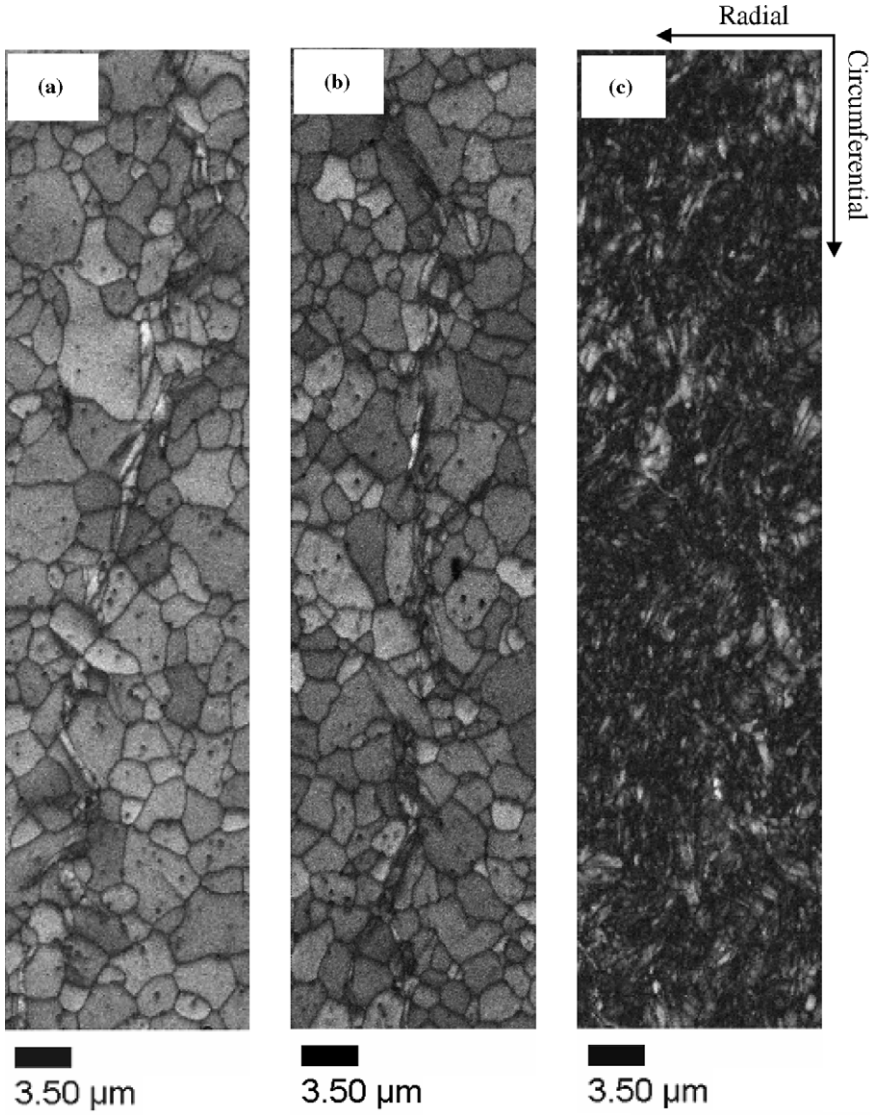

Fig. 2. Image quality (IQ) maps of Zircaloy-2 cladding tubes with different annealing conditions. Gray level in the maps represents relative intensity of the lattice strains: (a) RX1, (b) RX2, (c) SR1.

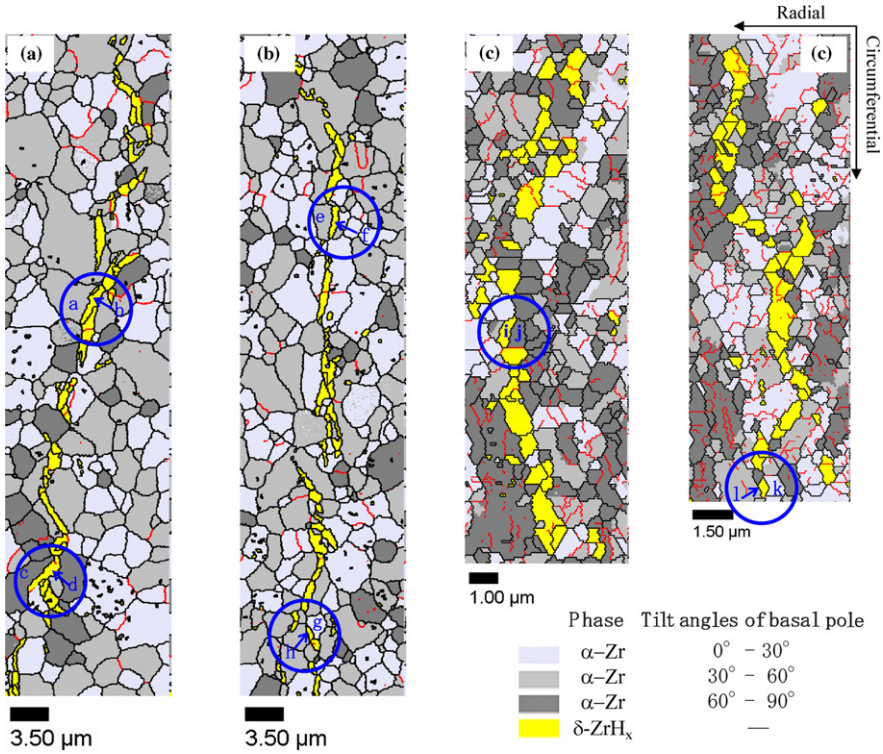

Fig. 3. Crystal orientation maps of α-Zr grains in Ziracaloy-2 cladding tubes. Three different gray levels of α-Zr grains indicate the tilt angles of the basal pole from the radial direction of the tube. Yellow grains are δ-ZrH_x. Black and red lines denote high- and low angle grain boundaries: (a) RX1, (b) RX2, (c) SR1.

tation angles of more than 15° and between 5° and 15°, respectively. These kinds of crystal orientation mapping with a spatial resolution of sub-micron size for polycrystalline bulk specimens have been realized only by recent EBSP technique. Comparing the grain size of α-Zr and grain boundary characteristics of the recrystallized and stress-relieved tubes, naturally the latter tube has smaller grains and much more numbers of low angle boundaries. Another important point is that more radial grains of the basal pole are seen for the two recrystallized tubes, compared to the stress-relieved tube, as seen in Fig. 3(a)–(c).

The EBSP measurements for the α-Zr matrix grains in the present three kinds of tubes (RX1, RX2, SR1) are summarized in Table 1. Almost the same grain sizes (~3 μm) and fractions of low-angle grain boundaries (5–6%) were obtained for the two recrystallized tubes of RX1 and RX2. On the other hand, the stress-relieved tube of SR1 had partially recrystallized small grains of about 1 μm with a fraction of low-angle boundaries of 26%, as seen in the crystal orientation map of Fig. 3(c). In addition to these grain characteristics, the microtexture in small areas of about 15×60 μm of each material were derived from the EBSP mapping data. Fig. 4 shows the (0 0 0 1) basal pole figures and inverse pole figures of the three tubes (|| radial direction), evaluated from the EBSP mapping data. Comparing the pole figures of RX1 and RX2, the radial texture of the basal plane in RX2 seems to be somewhat stronger than that of RX1. The basal poles in SR1 appear to be more diffused toward the circumferential direction.

The degree of macroscopic or average radial texture of cladding tubes is generally given in terms of f_r value by X-ray diffraction measurements (XRD), which represents the fraction of all basal poles oriented in the radial direction [29]. Since the present EBSP system did not equipped an evaluation software of f_r value, we adopted a radial texture parameter from the microscopic EBSP data, which is given as a percentage of the c-axis of α-Zr located within ±40° of the tube radial direction. The evaluated values of this index are given in Table 1, together with f_r values by XRD for the recrystallized

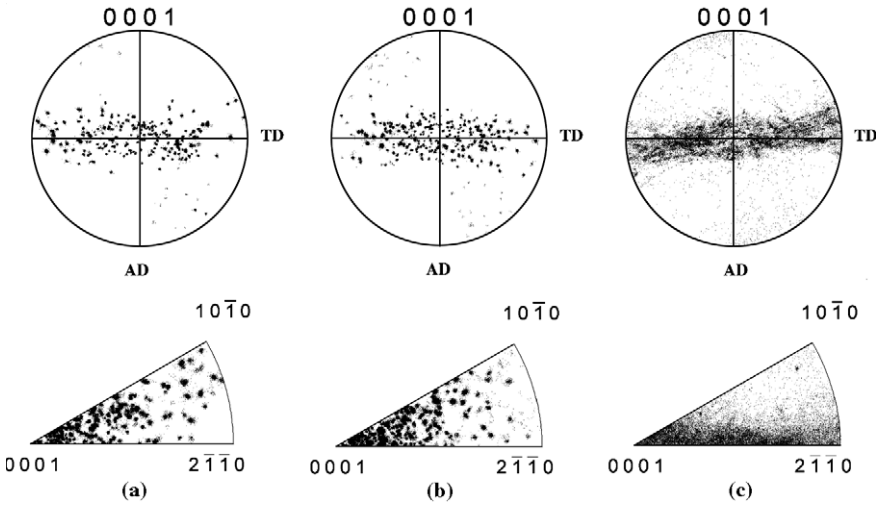

Fig. 4. Basal pole figures and inverse pole figures of Zircaloy-2 cladding tubes evaluated by EBSP (|| radial direction): (a) RX1, (b) RX2, (c) SR1.

tubes. RX2 has a stronger radial texture than RX1 on the basis both the presently defined radial texture parameter obtained by EBSP and the f_r value obtained by XRD. This may be partly due to the somewhat different tube reduction schedule for RX1 and RX2 provided from different tube vendors. The radial texture or f_r value of RX3 examined in the previous study seems to be almost equivalent with that of RX1.

The radial texture parameter of SR1 (44%) is certainly weaker than that of RX1 (60%), even though the two tubes with different final annealing temperatures were prepared from the same cold-worked Zircaloy-2 tube. This indicates that the more radial texture of the basal plane in the present recrystallized tube probably results from the rotation of small Zr grains during the recrystallization or grain growth process. In deed, a relatively strong radial texture of $\{11\bar{2}0\}$ or axial texture of $\{10\bar{1}0\}$ seen in the SR1 tube, change to a weak axial texture of $\{11\bar{2}0\}$ in the RX1 tube, as seen in the inverse pole figures of Fig. 4. A similar behavior has previously been reported for the effect of annealing temperature on the texture [29], using various Zircaloy-2 tubes with different tube reduction schedules: The position of the basal pole peaks shifted closer to the radial direction of the tube with increasing annealing temperature. Although this annealing texture was reported to be dependent firstly on the strain ratio during the final tube reduction, some other unknown factors may play an important role [29].

3.2. Hydride precipitation

3.2.1. Precipitation morphology

As seen in the micrographs in Fig. 1(a)–(c), strings of interlinked hydrides several tens to a hundred-μm long, orient generally in the circumferential direction of the tubes. In the current recrystallized Zircaloy-2 tubes with a radial texture of the basal pole, hydrides tend to precipitate and grow in the circumferential direction [30]. The hydride strings in the RX1 and RX2 tubes in Fig. 3(a) and (b) are composed of inter- and intra-granular hydrides of several μm, which are precipitated roughly in the circumferential direction, and interlink in a zigzag manner. The inter-granular hydrides precipitate in the grain boundaries and grow along the boundaries of one of two adjacent grains.

The large hydride strings seen in Fig. 1(a)–(c) are separated by a distance of at least several tens μm. Further microscopic examination by EBSP of Fig. 3 also confirms that the precipitation of small hydrides of sub-micron size is rarely seen around large hydride strings. This would be caused by a ripening mechanism of hydrides and/or a hydride growth mechanism in preferred sites and orientations. In other words, hydrides precipitate first at special sites in grains and grain boundaries where the hydrogen solid solubility at hydride precipitation is locally lower than at other regions. One of the mechanism for the lowering of the solubility, we proposed the tensile stress effect at local sites [26]. Slightly larger tensile stresses near the front

of hydride platelets may induce slightly lower hydrogen solubility, and accelerate hydride growth there. Consequently, the hydrogen concentration in solution near the hydride platelets becomes low, bringing about the prevention of new hydrides. This phenomenon may be related to the saturation of the width of hydride platelets or anisotropic growth of hydride platelets. As seen in Fig. 3, the maximum platelet width appears to be about 0.7–0.9 μm, which is almost the same as in the previous study [26].

From the EBSP maps for the RX1 and RX2 tubes in Fig. 3(a) and (b), the precipitation sites of hydrides 1 to 5–6 μm in size with different crystal orientations were classified into intra- or inter-granular type. The results, summarized in Table 2, show that the ratio of inter-/intra-granular sites is 1.7 for RX1 and 2.0 for RX2, respectively. These ratios are roughly consistent with existing EBSP results (precipitation ratio: 2.2) obtained using a recrystallized Zircaloy-2 tube of RX3 supplied by the third vendor [26]. These results indicate that hydrides tend to precipitate preferentially in the grain boundaries where a large number of lattice disorders exist, as seen in the IQ maps of Fig. 1(a) and (b). The present EBSP data clearly demonstrate that the inter-granular hydrides do not prefer special grain boundaries, such as basal and prism tilt boundaries suggested in earlier studies [31,32]. Rather, they usually precipitate in random grain boundaries and grow along the boundary of one of two adjacent grains.

In the case of the stress-relieved tube (SR1) of Fig. 3(c), many larger hydrides that attack and occupy small Zr grains about 1 μm in size, interlink in a zigzag manner and form hydride strings of several tens to hundred-μm in the circumferential direction of the tube. In addition to these larger hydrides, tiny hydrides (0.2–0.3 μm) appear to precipitate sometimes, both in the grains and grain boundaries of the SR1 tube. For the larger hydrides, we cannot judge the precipitation sites of intra- or inter-granular types because of the almost equivalent sizes of the hydrides and small Zr matrix grains. Nevertheless, both intra- and inter-granular sites could be available for hydride precipitation in the stress-relieved tube as well.

3.2.2. Hydride habit plane

The crystallographic relationships between micron-sized hydrides and the surrounding Zr grains for the two recrystallized (RX1, RX2) and one stress-relieved tube (SR1) were surveyed by means of the normal pole figure method used in our previous paper [26]. The crystal planes examined were (0001), $\{10\bar{1}7\}$, $\{10\bar{1}1\}$, $\{10\bar{1}0\}$ for the α-Zr matrix grains, and {111}, {100}, {110} for the δ-hydride grains. Assuming a tolerance angle of ±5° in a single crystal for the present EBSP data analyses, the coincidence between the crystallographic orientations of the hydrides and Zr grains was judged by a difference in angle of $<\pm 5°$.

In the case of the two recrystallized tubes RX1 and RX2, certain crystallographic relationships between the hydrides and the surrounding Zr grains were usually found in both intra- and inter-granular type hydrides. Examples of the pole figure coincidence between them are given in Fig. 5. The analytical locations in the figure correspond just to those in Fig. 3(a)–(c). The (a,b) and (c,d) locations of RX1 show the results of intra- and inter-granular precipitation types, respectively. For both locations, the $(0001)_\alpha \| \{111\}_\delta$ relationship is clearly found. In the case of RX2, the $\{10\bar{1}7\}_\alpha \| \{111\}_\delta$ relationship stands at (g,h) location, in addition to $(0001)_\alpha \| \{111\}_\delta$. On the basis of statistical numbers of analyses for the two recrystallized tubes, the most common relationship is $(0001)_\alpha \| \{111\}_\delta$ for both types of hydrides. The second habit plane is recognized to be $\{10\bar{1}7\}_\alpha \| \{111\}_\delta$. The $\{10\bar{1}7\}$ plane is tilted by 15° from the (0001) basal plane, and has hexagonal symmetry. No habit planes other than (0001) and $\{10\bar{1}7\}$ were found in the recrystallized

Table 2
Hydride grain size, precipitation site and habit plane in Zircaloy-2 cladding tubes evaluated by EBSP

Specimen	Hydride grain size (μm)	Ratio of inter-/intra-granular sites	Number of analyzing locations	Habit plane		
				(0001) (%)	$\{10\bar{1}7\}$ (%)	$\{10\bar{1}1\}$ (%)
RX1	1.1	1.7	25	92	8	0
RX2	1.2	2.0	21	86	14	0
RX3[a]	1.2	2.2	29	90	10	0
SR1	0.7	–	34	70	18	12

[a] Ref. [26].

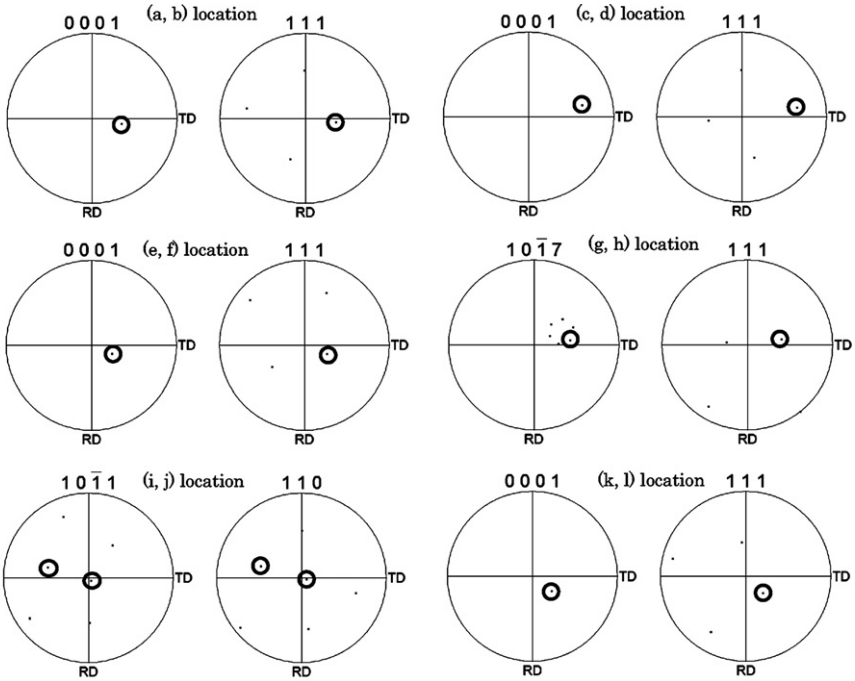

Fig. 5. Pole figure analysis results of α-Zr and δ-ZrHx for determination of hydride habit plane. Circles in the pole figures denote the coincidence of the crystallographic orientations.

tubes. The present results are completely consistent with those observed in other recrystallized Zircaloy-2 tubes in our previous paper [26]. Moreover, these primary and secondary habit planes of (0 0 0 1) and $\{1\,0\,\bar{1}\,7\}$ are in accordance with the TEM results in some of the literature on Zr alloy tubes [19–23].

In the case of the stress-relieved tube SR1, no clear crystallographic relationships were established between large hydrides and the surrounding Zr grains since hydrides about 0.7 μm in size attack almost the entire region of small Zr matrix grains of about 1 μm grain size. Therefore, the coincidence of the habit planes was derived from relatively smaller hydrides. The results were basically the same as for the case of the recrystallized tubes, except for $\{1\,0\,\bar{1}\,1\}_\alpha \| \{1\,1\,0\}_\delta$ with a low probability ((g, h) location). That is, the observation frequency of the habit planes in the stress-relieved tube was $(0\,0\,0\,1)_\alpha \| \{1\,1\,1\}_\delta \gg \{1\,0\,\bar{1}\,7\}_\alpha \| \{1\,1\,1\}_\delta > \{1\,0\,\bar{1}\,1\}_\alpha \| \{1\,1\,0\}_\delta$. Previous studies [9,13–15,17–19] have proposed other low-index planes, namely $\{1\,0\,\bar{1}\,1\}$ and $\{1\,0\,\bar{1}\,0\}$, for the hydride habit planes.

Table 2 summarizes the observation frequency of the hydride habit plane together with the number of locations analyzed. Table 2 also tabulates data on other recrystallized tube of RX3 reported in our previous paper [26]. For the three recrystallized tubes provided from different vendors, the primary habit plane was the (0 0 0 1) with a high frequency of about 90%, followed by the $\{1\,0\,\bar{1}\,7\}$ plane, with about 10%. By contrast, for the stress relieved tube SR1, which had the same tube reduction route as the recrystallized tube of RX1, the frequency of habit planes was ~70% for (0 0 0 1), ~20% for $\{1\,0\,\bar{1}\,7\}$, and ~10% for $\{1\,0\,\bar{1}\,1\}$. Statistical evaluations based on 20–30 analytical locations for each tube suggest that these results are relatively reproducible. The reason for the occurrence of the $\{1\,0\,\bar{1}\,7\}$ and $\{1\,0\,\bar{1}\,1\}$ planes in the stress-relieved tube may be related to its higher level of lattice strains or high density of dislocations, as seen in the IQ map of Fig. 1(c).

4. Conclusions

Precipitation morphology and habit plane of zirconium hydrides, and microscopic texture in three kinds of Zircaloy-2 fuel claddings were examined by electron backscattering diffraction patterns (EBSP). Two recrystallized claddings with a final annealing condition of 577 °C × 2 h were supplied by two different vendors. One stress-relieved cladding tube with an annealing condition of 480 °C × 3 h was prepared by annealing a cold-

worked tube, which had the same tube cold-reduction path as one of the recrystallized tubes.

(1) The EBSP image quality and crystal orientation mapping data revealed a clear difference in the recrystallization process between the stress-relieved and recrystallized tubes. About one third of all the grain boundaries in the stress-relieved tube were low angle boundaries with misorientation angles of 5–15°, while the fraction of low angle boundaries was only about 5% in the recrystallized tube. The average grain sizes of the former and latter tubes were 3 and 1 μm, respectively. The microscopic texture data obtained by EBSP were consistent with the macroscopic X-ray data. The Zr basal plane was observed to have a more radial texture in the case of the recrystallized tube as compared to the stress-relieved tube, even though both tubes had the same tube reduction path. This indicates the rotation of small Zr grains during the grain growth process.

(2) The circumferentially oriented hydride strings in the recrystallized and stress-relieved tubes were composed of micron-sized inter- and intra-granular hydrides, which interlinked in a zigzag manner. The inter-granular hydrides grew along the grain boundaries, on the surface of one of two adjacent grains. For the recrystallized tubes, the frequency of precipitation and stable growth sites in inter-granular hydrides was about twice as large as that in intra-granular sites. In the case of the stress-relieved tubes, smaller hydrides of sub-micron size precipitated in the grain boundaries and within grains. However, the above ratio could not be derived accurately because of the almost equivalent sizes of larger hydrides and smaller Zr grains of about 1 μm.

(3) The observation frequency of the habit planes of hydrides, which was evaluated from the statistical amounts of pole figure analyses of EBSP between the hydrides and surrounding Zr matrix grains, decreased in the order $(0001)_\alpha \| \{111\}_\delta \gg \{10\bar{1}7\}_\alpha \| \{111\}_\delta$ for the recrystallized tubes. In addition to these primary and secondary relationships, the habit plane $\{10\bar{1}1\}_\alpha \| \{110\}_\delta$ with a low probability was found in the case of the stress-relieved tube.

References

[1] D.O. Northwood, U. Kosasih, Int. Met. Rev. 28 (1983) 92.
[2] B. Cox, J. Nucl. Mater. 170 (1990) 1.
[3] K. Edsinger, J.H. Davies, R.B. Adamson, Zirconium in the Nuclear Industry, ASTM STP 1354, 2000, p. 316.
[4] K. Edsinger, Proceedings of the International Topical Meeting on Light Water Reactor Fuel Performance, Park City, 10–13 April 2000, p. 523.
[5] H. Hayashi, Y. Tsukuda, S. Shimada, Y. Etoh, ENS TopFuel 2003, Wurzburg, Germany, 16–19 March 2003.
[6] S. Shimada, H. Hayashi, Y. Tsukuda, Y. Etoh, J. Nucl. Mater. 327 (2004) 97.
[7] T. Fuketa, H. Sasajima, Y. Tsuchiuchi, Y. Mori, T. Nakamura, K. Ishijima, Proceedings of the International Topical Meeting on Light Water Reactor Fuel Performance, Portland, Oregon, 2–6 March 1997, p. 669.
[8] T. Nakamura, K. Kusagaya, T. Fuketa, H. Uetsuka, Nucl. Technol. 138 (2002) 246.
[9] C.E. Ells, J. Nucl. Mater. 28 (1968) 129.
[10] J.J. Kearns, C.R. Woods, J. Nucl. Mater. 20 (1966) 241.
[11] N. Nagai, K. Fujita, Kikai-Gijyutsu 31 (1983) 70 (in Japanese).
[12] M. Veleva, S. Arsene, M. Record, J.L. Bechade, J. Bai, Metall. Mater. Trans. A 34 (2003) 567.
[13] J.E. Bailey, Acta Metall. 11 (1963) 267.
[14] D.O. Northwood, R.W. Gilbert, L.E. Bahen, Canadian Metall. Quarterly 14 (1975) 123.
[15] G.C. Weatherly, Acta Metall. 29 (1981) 501.
[16] F.W. Kunz, A.E. Bibb, Trans. AIME 218 (1960) 133.
[17] V.S. Alunachalam, B. Lehtinen, G. Ostberg, J. Nucl. Mater. 21 (1967) 241.
[18] D.G. Westlake, E.S. Fisher, Trans. AIME 224 (1962) 254.
[19] H.M. Chung, R.S. Daum, J.M. Hiller, M.C. Billone, Zirconium in the Nuclear Industry, ASTM STP 1423, 2002, p. 561.
[20] V. Perovic, G.C. Weatherly, Acta Metall. 31 (1983) 1381.
[21] V. Perovic, G.C. Weatherly, J. Nucl. Mater. 126 (1984) 160.
[22] Y.S. Kim, Y. Perlovich, M. Isaenkova, S.S. Kim, Y.M. Cheong, J. Nucl. Mater. 297 (2001) 292.
[23] S. Neogy, D. Srivastava, R. Tewari, R.N. Singh, G.K. Dey, S. Banerjee, J. Nucl. Mater. 322 (2003) 195.
[24] W.J. Babyak, Trans. Metall. Soc. AIME 239 (1967) 252.
[25] D.G. Westlake, J. Nucl. Mater. 26 (1968) 208.
[26] K. Une, K. Nogita, S. Ishimoto, K. Ogata, J. Nucl. Sci. Technol. 41 (2004) 731.
[27] K. Une, S. Ishimoto, J. Nucl. Mater. 322 (2003) 66.
[28] K. Une, S. Ishimoto, J. Nucl. Sci. Technol. 41 (2004) 949.
[29] N. Nagai, T. Kakuma, K. Fujita, Zirconium in the Nuclear Industry, ASTM STP 754, 1982, p. 26.
[30] H. Abe, K. Takabe, A. Uehara, H. Anada, M. Furugen, Zirconium in the Nuclear Industry, ASTM STP 1354, 2000, p. 425.
[31] J.F.K. Amber, J. Nucl. Mater. 28 (1968) 237.
[32] Y. Mishima, S. Ishino, H. Kawanishi, Congres Int. L'Hydrogene dans les Metaux 2 (1972) 469.